Spectral Bifurcation and Anomalous Supercurrent in Dissipative Topological Insulator-based Josephson Junctions

Ardamon Sten [1,*] Paramita Dutta [2,†] and Sudeep Kumar Ghosh [1,‡]

[1] *Department of Physics, Indian Institute of Technology, Kanpur 208016, India*
[2] *Theoretical Physics Division, Physical Research Laboratory, Navrangpura, Ahmedabad-380009, India*

(Dated: December 3, 2025)

The interplay between topological protection and dissipation constitutes a critical frontier in the realization of hybrid quantum devices. Here, we investigate the transport signatures in a dissipative topological insulator-based Josephson junction, a platform that directly probes the competition between quantum coherence and loss. We model dissipation by coupling a 'lossy' metallic lead to the junction, described effectively by a non-Hermitian Hamiltonian derived using the Lindblad formalism. We observe that the junction exhibits an asymmetric complex Andreev spectrum, where the imaginary energy component imposes a finite lifetime on the quasi-bound states. Furthermore, beyond specific phase intervals, the real component of the spectrum bifurcates: one branch merges with the continuum, while the other penetrates just below the superconducting gap. Crucially, the characteristic zero-energy crossing shifts away from $\phi = \pi$ and acquires a non-zero imaginary component; consequently, the associated Majorana bound states acquire a finite lifetime, signaling a loss of robustness against dissipation. Finally, this spectral asymmetry drives an anomalous supercurrent, manifested as a non-vanishing current at zero phase difference. Our results reveal how dissipation fundamentally reshapes superconducting transport in topological junctions, opening new directions for dissipation-engineered quantum devices.

Josephson junctions (JJs) play a pivotal role in superconducting electronics, offering a versatile tool for probing quantum transport, topological states, and unique superconducting behaviors [1]. In conventional Hermitian JJs, the superconducting phase difference determines the current-phase relationship (CPR), which is typically 2π-periodic and sinusoidal in 'short' junctions [2]. These junctions are fundamental to technologies such as Superconducting Quantum Interference Devices (SQUIDs) and single-photon detectors [3]. Topological insulator-based Josephson junctions (TIJJs) provide an ideal setting for realizing exotic quantum states [4–7], where proximity-induced superconductivity on the surface of a 3D topological insulator (3DTI) induces helical Andreev bound states (ABSs) [4, 8, 9]. These junctions support non-chiral Majorana modes [4, 10, 11], leading to 4π-periodic Josephson effects [4, 9, 12, 13].

Dissipation is an intrinsic aspect of real-world Josephson junctions, where non-Hermitian Hamiltonians capture the effects of environmental coupling [14–19]. In non-Hermitian Josephson junctions (NH-JJs), dissipation generates complex spectra and exceptional points (EPs), producing behavior absent in Hermitian systems [14, 16, 17, 20]. Although EPs in the ABS spectrum may leave no clear imprint on static quantities such as the DC Josephson current [17], they do manifest in dynamical observables like the current susceptibility [17] and in thermodynamic measures such as entropy [20]. However, the impact of non-Hermiticity on topological Josephson junctions remains largely unexplored, particularly in systems where dissipation competes with topological protection.

In this work, we address the central question: how does dissipation caused by coupling a 'lossy' metallic lead [14, 21] at the junction, affect the quantum transport properties of TIJJs? To explore this, we model the dissipative effects of the lead by an effective non-Hermitian Hamiltonian [16, 22] and investigate transport in a non-Hermitian planar Josephson junction on the surface of a 3DTI (NH-TIJJs), as illustrated schematically in Fig. 1. Here, proximity-induced superconductivity intertwines with non-Hermitian effects, offering a unique platform to study the interplay between dissipation and topological superconductivity.

Effective model of a NH-TIJJ: The NH-TIJJ in Fig. 1 consists of two s-wave singlet superconductors with identical gap Δ and phases ϕ_L and ϕ_R on the left and right, respectively. Dissipation due to the 'lossy' lead [14, 21]
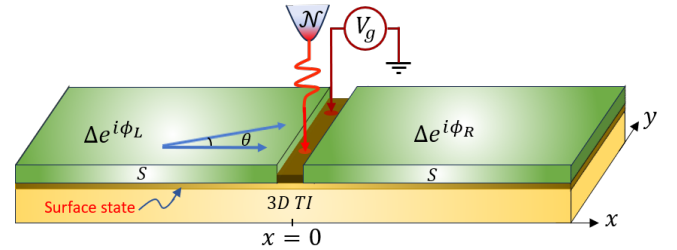

FIG. 1. **Schematic of a non-Hermitian planar TIJJ:** A 'short' TIJJ formed by placing two bulk s-wave singlet superconductors on the surface of a 3DTI. A top gate and a 'lossy' metallic lead ($\mathcal{N}$) are attached at the junction ($x = 0$), where the gate modifies the potential barrier via an applied voltage V_g and the lead introduces dissipation due to coupling to an electron reservoir.

* ardamons21@iitk.ac.in
† Jointly supervised this work; paramita@prl.res.in
‡ Jointly supervised this work; skghosh@iitk.ac.in

connected to an electron reservoir is modeled in a minimal way, within the Lindblad formalism neglecting quantum jumps [23, 24] (see Appendix A for details), by an imaginary potential barrier at the junction [16]. The combined effect of the top gate and the lead is therefore captured by a complex contact junction potential barrier: $U(x) = (V_1 - iV_2)\delta(x)$, where $V_1 > 0$ represents the real barrier strength tunable by the applied gate voltage V_g and $V_2 > 0$ accounts for the imaginary barrier strength induced by the lead.

Assuming tunnel coupling between the superconductors and the 3DTI surface state [4, 8, 25, 26], the physics of the proximity-induced superconductivity on the surface state can be described by the effective Bogoliubov-de Gennes (BdG) Hamiltonian [4, 8]:

$$\mathcal{H}_{\text{eff}} = \Phi^\dagger H_{\text{BdG}} \Phi ,$$

$$H_{\text{BdG}} = \begin{bmatrix} \frac{\hbar}{i}v_F\boldsymbol{\sigma}\cdot\nabla - \mu - \Gamma(\epsilon) & \tilde{\Delta}(\epsilon)i\sigma_y e^{i\phi_{L,R}} \\ -\tilde{\Delta}(\epsilon)i\sigma_y e^{-i\phi_{L,R}} & \frac{\hbar}{i}v_F\boldsymbol{\sigma}^*\cdot\nabla + \mu - \Gamma(\epsilon) \end{bmatrix} ,$$

$$\tilde{\Delta}(\epsilon) = \frac{i\Gamma_0\Delta}{\sqrt{\epsilon^2 - \Delta^2}} , \Gamma(\epsilon) = \frac{i\Gamma_0\epsilon}{\sqrt{\epsilon^2 - \Delta^2}} , \Gamma_0 = \pi t^2\mathcal{D}_0; \quad (1)$$

written in the Nambu basis $\Phi^\dagger = (\varphi_\uparrow^\dagger, \varphi_\downarrow^\dagger, \varphi_\uparrow, \varphi_\downarrow)$ with $\varphi_s^\dagger$ being the electron creation operator with spin $s = \uparrow, \downarrow$. μ is the chemical potential of the superconductor, v_F is the Fermi velocity of the surface states of the 3DTI and σ_i ($i = 1, 2$) are the Pauli matrices in spin space. $\tilde{\Delta}(\epsilon)$ is the proximity induced superconducting pairing potential which is a function of the Bogoliubov quasiparticle energy ϵ, $\Gamma(\epsilon)$ is the shift in energy of the quasiparticles due to tunneling with amplitude t, and Γ_0 is the tunneling energy scale that determines the tunneling rate. $\mathcal{D}_0$ is the density of states of the superconductors in the normal state. The proximitized superconductivity on the 3DTI surface is determined by the tunneling energy Γ_0, in the tunneling regime ($\Gamma_0 \ll \Delta$) the induced gap is much smaller than the parent s-wave gap and in the strong proximity limit ($\Gamma_0 = \Delta$) the pairing potential is equal to that of the parent superconductor. In this work, we investigate the transport properties in both of these regimes to see whether any new feature is observed in the tunneling regime.

To investigate transport in the "short" NH-TIJJ (Fig. 1), assuming the width of the junction much smaller than the coherence length of the superconductors, we consider $\phi_L = 0$ and $\phi_R = \phi$ without loss of generality. In this limit, the physics of the system can be described by [8]:

$$[H_{\text{BdG}}(\boldsymbol{r}) + (V_1\tau_z - iV_2\tau_0)\sigma_0]\Psi(\boldsymbol{r}) = \epsilon\Psi(\boldsymbol{r}) , \quad (2)$$

where, τ_z is the third Pauli matrix in the Nambu space, σ_0 is the 2×2 identity matrix and $\Psi(\boldsymbol{r}) = \left[\psi_{\uparrow,\epsilon}(\boldsymbol{r}), \psi_{\downarrow,\epsilon}(\boldsymbol{r}), \psi_{\uparrow,-\epsilon}^*(\boldsymbol{r}), \psi_{\downarrow,-\epsilon}^*(\boldsymbol{r})\right]^T$ is the Nambu spinor wavefunction. Quasiparticles enter the barrier from the left at an angle of incidence $\theta \in [-\pi/2, \pi/2]$ and we assume translational invariance along the y-direction.

Klein tunneling is insensitive to the precise form of the barrier [8, 27], so the specific shape of the potential does not matter for our analysis; only the influence of non-Hermiticity is relevant.

Complex helical ABSs and CPRs: The properties of the ABSs in the NH-TIJJ can be obtained by solving Eq. (2). Since wavefunctions of the ABSs decay exponentially as $|x| \to \infty$, with translational invariance in the y-direction, the wavefunctions have the general form: $\Psi(\boldsymbol{r}) = \sum_{k_y} \psi_{k_y}(x)e^{ik_y y}$ (see Appendix B for explicit forms of the ABS wavefunctions within the Andreev approximation). Integrating Eq. (2) around $x = 0$ and defining $Z = Z_1 - iZ_2$ where $Z_{1,2} = V_{1,2}/(\hbar v_F)$ characterize the potential barrier strengths, we get the boundary condition,

$$\psi_{k_y}(0_-) = [1 + iZ_1\tau_z\sigma_x + Z_2\tau_0\sigma_x]\psi_{k_y}(0_+) , \quad (3)$$

which leads to an equation in terms of $\mathcal{E}/\tilde{\Delta}$ (see Appendix B):

$$-4iZ_2\cos(\theta)\frac{\mathcal{E}}{\tilde{\Delta}}\sqrt{1 - \left(\frac{\mathcal{E}}{\tilde{\Delta}}\right)^2} = \mathcal{F}(\theta, \phi) - 2T_2\left(\frac{\mathcal{E}}{\tilde{\Delta}}\right)^2 . \quad (4)$$

Here, $\mathcal{F}(\theta, \phi) = (1 + Z_1^2 - Z_2^2)\cos^2(\theta)\cos(\phi) + (Z_1^2 + Z_2^2)(1 + \sin^2(\theta)) + \cos^2(\theta) + 2Z_1Z_2\cos^2(\theta)\sin(\phi)$, $T_2 = Z_1^2 + Z_2^2 + \cos^2(\theta)$, $\mathcal{E}(\epsilon) = \epsilon + i\Gamma(\epsilon)$ and $\tilde{\Delta} = \tilde{\Delta}(\epsilon)$. The above equation can be rearranged into a quadratic equation in the variable $y = \left|\frac{\mathcal{E}}{\Delta}\right|^2$ as $Ay^2 + By + C = 0$ giving the solutions

$$\left|\frac{\mathcal{E}}{\tilde{\Delta}}\right|^2 = \frac{-B \pm \sqrt{B^2 - 4AC}}{2A} , \quad (5)$$

where $A = 4Z_2^2\cos^2(\theta) - T_2^2$, $B = \mathcal{F}(\theta, \phi)T_2 - 4Z_2^2\cos^2(\theta)$, $C = -\mathcal{F}^2(\theta, \phi)/4$. In the case of strong proximity effect, $\mathcal{E}$ and $\tilde{\Delta}$ are independent of the quasiparticles energy ϵ and the induced gap can be treated as constant. In this limit, Eq. (5) can be interpreted as the bound state solutions for the TIJJ whose induced gap is equal to that of the parent superconductor (see Appendix B for more discussion). Denoting the R.H.S of Eq. (5) as $\mathcal{S}(\theta, \phi)$, we substitute the expressions of $\mathcal{E}$ and $\tilde{\Delta}$ and arrive at the following equation for the bound states in terms of $\alpha = |\frac{\epsilon}{\Delta}|$ in the tunneling regime

$$\alpha^2(1 - \alpha^2) = \gamma^2\left(\sqrt{\mathcal{S}(\theta, \phi)} - \alpha\right)^2 , \quad (6)$$

where $\gamma = \Gamma_0/\Delta \ll 1$ is a dimensionless parameter characterizing the tunneling strength. We seek solutions of Eq. (6) in powers of γ [8]: $|\epsilon/\Delta| = c_1\gamma + c_2\gamma^2 + c_3\gamma^3$, where c_1, c_2 and c_3 are unknown complex coefficients. Then in the 'short' junction limit, we obtain two branches (labeled by $\pm$) of complex ABS spectrum with energies (see Appendix B for details):

$$\frac{E_b^\pm(\theta, \phi)}{\Delta} = \pm\left[(\gamma - \gamma^2 + \gamma^3)\mathcal{S}^{\frac{1}{2}}(\theta, \phi) + \frac{\gamma^3}{2}\mathcal{S}^{\frac{3}{2}}(\theta, \phi)\right] . \quad (7)$$
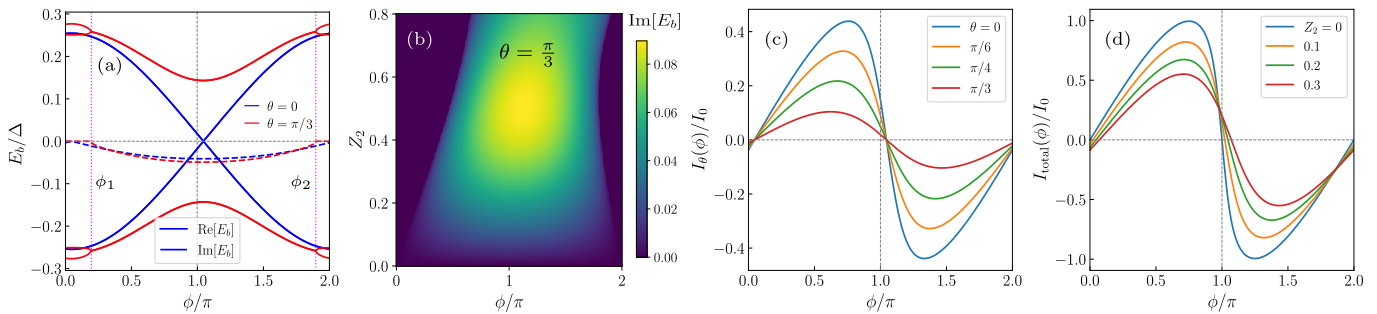
FIG. 2. **Characteristics of the NH-TIJJ for a complex barrier ($Z_1 \neq 0$, $Z_2 \neq 0$) in the tunneling limit ($\Gamma_0 \ll \Delta$):** (a) The real (solid lines) and imaginary (dashed lines) parts of the Andreev spectrum of the NH-TIJJ as a function of the phase difference ϕ plotted for different angles of incidence θ taking the imaginary barrier parameter $Z_2 = 0.2$. The ϕ_1 and ϕ_2 denote the GEPs, beyond which the real part of the spectrum exits the gap and the imaginary part of the spectrum vanishes. (b) Variation of the imaginary part of the spectrum as a function of ϕ and Z_2 for the incident angle $\theta = \pi/3$, the boundary of the dark purple region demonstrates the asymmetric gap-exit points in the spectrum. (c) The zero temperature angle-resolved current $I_\theta(\phi)$ plotted as a function of ϕ for different angles of incidence. (d) The total supercurrent $I_{\text{total}}(\phi)$ as a function of ϕ for different barrier parameters. We have chosen the real barrier parameter $Z_1 = 0.4$, tunneling parameter $\gamma = 0.3$ and $I_0 = eN\Gamma_0/(2\hbar)$ with N being the number of open channels.

The real parts of $E_b^\pm$ represent physical energies of the ABSs while the negative imaginary part of $E_b^\pm$ represents the broadening of the energy levels due to non-Hermiticity [16, 28], the positive imaginary branch signifies pumping of quasiparticles from the reservoir [29] and therefore does not represent a physical solution for dissipative systems. The variation of the ABS spectrum for different angles of incidence θ is shown in Fig. 2(a). Before discussing the features introduced by non-Hermiticity, we first remind ourselves of the ABS characteristics in the Hermitian case; the spectrum for normal incidence ($\theta = 0$) is gapless and features a zero-energy crossing at $\phi = \pi$ which corresponds to two Majorana bound states whose spinors are related by time-reversal symmetry and also preserve Klein tunneling [8]. The spectrum for oblique incidence ($\theta \neq 0$), however, features an angle-dependent gap and lacks time-reversal symmetry protection and thus experience scattering by the potential barrier.

In the non-Hermitian case, the normally incident quasiparticles feature a spectrum whose real part is gapless but the zero-energy crossing is shifted away from $\phi = \pi$ in contrast to the Hermitian case. There is also a finite imaginary component accompanying the real counterpart which indicates that Klein tunneling, which exists for normal incidence in the Hermitian case [8], is not robust against dissipation. The shift of the zero-energy crossing along the ϕ axis makes the spectrum asymmetric with respect to $\phi = \pi$ over the interval $\phi \in [0, 2\pi]$. Moreover, the finite imaginary component introduces a finite lifetime for the bound states, rendering the associated Majorana bound states unstable in the presence of non-Hermiticity. This can be understood as a purely non-Hermitian effect where dissipation affects the Kramers degeneracy and can induce effects such as splitting of spectral functions of Kramers degenerate states [30].

Meanwhile, obliquely incident quasiparticles experi-

ence the effect of non-Hermiticity in two qualitatively new effects: (i) broadening of the quasi-ABSs energy levels which means that the bound states have acquired a finite lifetime [31] and (ii) a fully gapped quasi-ABS spectrum which beyond a certain interval $\phi \in [\phi_1, \phi_2]$, the real part of both particle and hole spectrum bifurcates into two branches with one branch going above the induced gap (supra-gap) and the other going below it (sub-gap). We call the points ϕ_1 and ϕ_2 on the ϕ-axis where the real part of the spectrum exits the gap as gap-exit points (GEPs), the imaginary part of the spectrum vanishes beyond these points as shown in Fig. 2(b) and the position of the GEPs, demonstrated by the boundary of the dark purple region, is asymmetric about $\phi = \pi$ in the interval $\phi \in [0, 2\pi]$. Since the normally incident quasi-particles do not experience scattering from the real barrier, therefore the bifurcation is demonstrated only in oblique incidence and is absent for normal incidence.

To calculate the Josephson current, we employ the Furusaki-Tsukada (FT) formula [32, 33] which provides an alternative approach to compute the supercurrent in
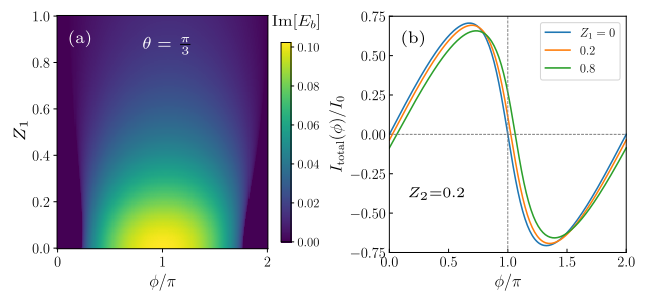

FIG. 3. **Characteristics of the NH-TIJJ for fixed $Z_2 = 0.2$ in the tunneling limit:** Variation of the (a) imaginary part of the Andreev spectrum as a function of Z_1 and ϕ, and (b) total current as a function of ϕ for different values of Z_1.
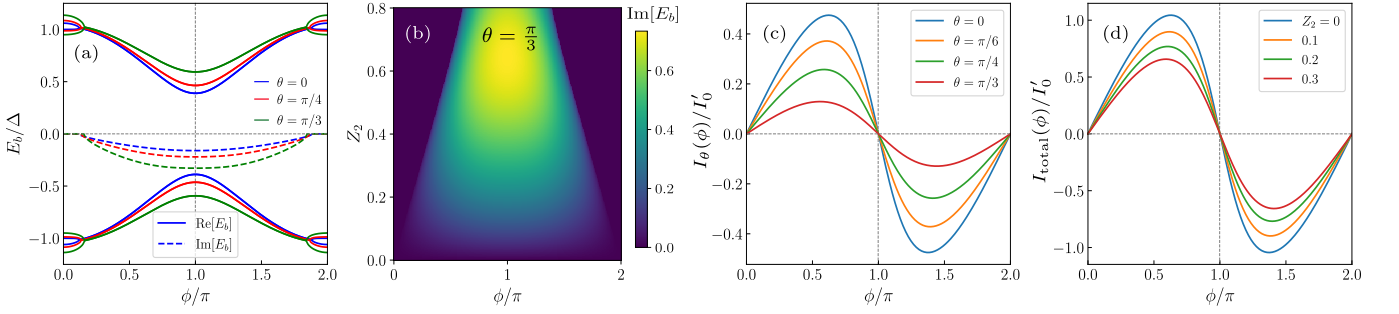
FIG. 4. **Characteristics of the ordinary NH-JJ for a complex barrier** ($Z_1 \neq 0, Z_2 \neq 0$): (a) The real (solid lines) and imaginary (dashed lines) parts of the Andreev spectrum of the 2D NH-JJ as a function of the phase difference ϕ plotted for different angles of incidence θ taking the imaginary barrier parameter $Z_2 = 0.2$. (b) Variation of the imaginary part of the spectrum as a function of ϕ and Z_2 for the incident angle $\theta = \pi/3$, the boundary of the dark purple region demonstrates the symmetric gap-exit points in the spectrum. (c) The angle-resolved current $I_\theta(\phi)$ plotted as a function of ϕ for different angles of incidence at zero temperature and $Z_2 = 0.2$. (d) The total supercurrent $I_{\text{total}}(\phi)$ as a function of ϕ for different barrier parameters. Here, $I'_0 = e\Delta/\hbar$ and $Z_1 = 0.4$.

terms of the Andreev reflection processes as,

$$I_\theta(\phi) = \frac{e}{\hbar} k_B T \sum_{\omega_n} \frac{\tilde{\Delta}(\omega_n)}{\Omega_n} [r_{he}(\phi, \omega_n) - r_{eh}(\phi, \omega_n)] , \quad (8)$$

where analytic continuation for the energy is done as $E \to i\omega_n$ in terms of the Matsubara frequencies $\omega_n = (2n+1)\pi/k_B T$ with n being an integer, the parameter $\Omega_n = \sqrt{\omega_n^2 + \Delta^2}$, r_{he} is the Andreev coefficient for an incoming electron-like quasiparticle being reflected as a hole-like quasiparticle and r_{eh} is the corresponding coefficient for the reverse process for a hole-like quasiparticle. In the zero-temperature limit $T \to 0$, the summation over Matsubara frequencies can be replaced by an integration over real energy as $k_B T \sum_{\omega_n} \to \frac{1}{2\pi} \int d\omega$ on performing the analytic continuation $i\omega_n \to \omega + i0^+$. We note that the existing supercurrent formulae for NH systems used to evaluate the current in systems with EPs [17, 20] incur a divergence of the angle-resolved current at the GEPs, therefore to resolve these divergences we use the FT formula and limit our analysis within the subgap approximation ($|\omega| < \Delta$). The variation of the angle-resolved current $I_\theta(\phi)$ for different θ at zero temperature within the subgap approximation is shown in Fig. 2(c). The current is 2π-periodic and exhibits an 'anomalous' behavior where the supercurrent is non-zero at $\phi = 0, 2\pi$ for all angles of incidence. For normal incidence, the current changes sign smoothly and does not exhibit the abrupt discontinuity at the zero-energy crossing as in the Hermitian case, which highlights the contribution of the imaginary part of the spectrum in reshaping and smoothing the CPRs. For oblique incidence, in addition to the mentioned characteristics, the critical current decreases with increasing θ indicating that the effect of non-Hermiticity is more effective with increasing obliqueness.

The total equilibrium Josephson current (I_{total}) can be obtained as:

$$I_{\text{total}}(\phi) = \int_{-\pi/2}^{\pi/2} I(\phi, \theta) \cos(\theta) d\theta . \quad (9)$$

The CPR for the NH-TIJJ is shown in Fig. 2(d) for different values of the non-Hermiticity strength Z_2. The CPR features a 2π-periodic, non-sinusoidal, anomalous current which is asymmetric about $\phi = \pi$ carrying the signature of the asymmetry of the ABSs shown in Fig. 2. The critical current is maximum for the Hermitian case ($Z_2 = 0$) and decreases with increasing Z_2 for a fixed Z_1 due to quasiparticles experiencing decoherence and escaping to the reservoir. The main feature of the CPR is its asymmetry about the phase difference $\phi = \pi$ and its non-zero value at $\phi = 0, 2\pi$, this anomalous behavior of the supercurrent stems from the asymmetry in the Andreev spectrum whereby the corresponding subgap contribution outside the GEPs is also asymmetric, thus resulting in an anomalous CPR. The asymmetry is an outcome of the interplay between the real barrier and non-Hermiticity, as is evident in Fig. 3(a) where the GEPs (boundary of dark purple region) are initially symmetric when $Z_1 = 0$ and become asymmetric when $Z_1 \neq 0$. The variation of the CPR for different values of the real barrier Z_1 for a fixed Z_2 is shown in Fig. 3(b), the critical current is maximum for $Z_1 = 0$ and decreases as Z_1 increases due to enhanced normal reflection. Note that the anomalous behavior is absent when $Z_1 = 0$ since asymmetry in the spectrum requires both the barrier parameters Z_1 and Z_2 to be non-zero.

Comparison with 'ordinary' NH-JJs: We consider an 'ordinary' planar NH-JJ, where the 3DTI in Fig. 1 is replaced by an 'ordinary' metal, to highlight the special features of the NH-TIJJ. Proceeding in a similar way, in the 'short' junction limit within the Andreev approximation, the ABS energies are given by (see Appendix C for details),

$$g_2(\theta, \phi) \left(\frac{E_b}{\Delta'}\right)^2 = g_1(\theta, \phi) Z^2 + \cos^4(\theta) \cos^2\left(\frac{\phi}{2}\right)$$

$$+ 2Z_1^2 \cos^2(\theta) \pm 2Z_2 \sqrt{g_1(\theta, \phi) \cos^2\left(\frac{\phi}{2}\right) - Z_1^2}. \quad (10)$$

Here, $Z^2 = (Z_1^2 + Z_2^2)$ with the dimensionless barrier parameters defined as $Z_i = \frac{mV_i}{\hbar^2 k_F}$ in this case, $g_1(\theta, \phi) = Z^2 - \cos^2(\theta)\sin^2\left(\frac{\phi}{2}\right)$, $g_2(\theta, \phi) = \left[Z^2 + \cos^2(\theta)\right]^2 - 4Z_2^2 \cos^2(\theta)$ and Δ' is the induced superconducting gap amplitude in the metal.

The full Andreev spectrum is shown in Fig. 4 and it shares features similar to that of the NH-TIJJ. The spectrum for different incident angles θ is shown in Fig. 4(a). The spectrum is complex with the real branches showing bifurcation beyond the interval $\phi \in [\phi_0, 2\pi - \phi_0]$ where $\phi_0(Z, \theta) = 2\sin^{-1}\left(\frac{\sqrt{2}Z_2}{\sqrt{\cos^2(\theta)+Z^2}}\right)$, both the energy gap between the real branches and the behavior of the imaginary part are strongly dependent on the angle of incidence. $\text{Im}[E_b]$ increases with increasing θ which indicates that the effect of non-Hermiticity increases with increasing θ consistent with the NH-TIJJ case (see Fig. 2). The boundary of the purple region (see Fig. 4(b)) where the imaginary part of the spectrum for $\theta = \pi/3$ is plotted as a function of the imaginary potential strength Z_2 and θ demonstrates the position of the GEPs which are symmetric about $\phi = \pi$ in contrast to the asymmetric feature in NH-TIJJ (see Fig. 2(b)). Hence, the NH-JJ and NH-TIJJ share a common qualitative behavior in that the Andreev spectrum is complex with the real parts exhibiting bifurcation beyond the GEPs while also exhibiting contrasting behaviors such as the absence of zero-energy states in an NH-JJ and an asymmetric spectrum in the NH-TIJJ.

The variation of the angle-resolved Josephson current $I_\theta(\phi)$ in Eq. (8) for different angles of incidence is shown in Fig. 4(c). We note that in stark contrast to the NH-TIJJ, the angle-resolved current does not exhibit the anomalous behavior since the Andreev spectrum of the NH-JJ is symmetric. The total current shown in Fig. 4(d) for different values of Z_2 features a 2π-periodic, non-sinusoidal CPR whose critical current decreases with increasing Z_2. The absence of anomalous behavior of the supercurrent in the case of NH-JJ is due to the lack of any Kramers degeneracy in the spectrum, thus there is no

interplay with non-Hermiticity to create the asymmetry in the spectrum as in the case of a NH-TIJJ.

Comparison with CPR from ABS formula: The alternative supercurrent formulae for NH systems [17, 20] with EPs are not able to resolve the divergence of the supercurrent at the GEPs in our system as mentioned earlier. Therefore we calculate the supercurrent from an ABS formula derived from the polar Green's function [28] focusing only on the subgap contribution and compare with the CPR computed from the FT formula. The angle-resolved Josephson current at zero temperature from this ABS formula is given by [28]:

$$I_\theta(\phi) = -\frac{2e}{\hbar}\frac{1}{\pi}\left\{(\partial_\phi \epsilon)\int_{-\Delta}^{\Delta} d\omega \frac{\tanh(\beta\omega/2)\,\lambda}{(\omega+\epsilon)^2+\lambda^2} \right.$$
$$\left. -(\partial_\phi \lambda)\int_{-\Delta}^{\Delta} d\omega \frac{\tanh(\beta\omega/2)\,(\omega+\epsilon)}{(\omega+\epsilon)^2+\lambda^2}\right\} \quad (11)$$

after decomposing the Andreev spectrum as $E_b = \epsilon - i\lambda$ with ϵ and λ being the real and imaginary part of the spectrum respectively. The resulting CPR is plotted in Fig. 5 for both the NH-JJ and the NH-TIJJ in the strong-proximity regime. Within this subgap approximation, the ABS formula predicts 'Josephson gaps', intervals of vanishing supercurrent [16]. However, a significant discrepancy exists between these two formulas, particularly near the GEPs where the FT result shows no such gaps as shown in Fig. 5. This mismatch arises because the ABS formula captures only the contribution from the bound-state spectrum (Green's function poles), yielding zero current where bound states are absent (beyond GEPs). In non-Hermitian systems, however, a critical contribution stems from the Green's function branch cuts [28]. Unlike the ABS formula, the FT approach incorporates all the reflection processes, thereby recovering a finite supercurrent outside the GEPs as well.

Summary and conclusions: We have investigated the quantum transport properties of a dissipative Josephson junction on the surface of a 3DTI, aiming to elucidate the interplay between dissipation and topological protection. Dissipation, modeled via an effective non-Hermitian Hamiltonian within the Lindblad formalism, arises from coupling to a 'lossy' metallic lead [14, 21] at the junction to an electron reservoir. Our study reveals that the Andreev bound state (ABS) spectrum is complex and merges into the continuum regime beyond certain interval of the phase difference. The spectrum also exhibit an asymmetry arising from the interplay of normal scattering and non-Hermiticity. This asymmetry in the spectrum results in the anomalous behavior of the CPR, where a finite supercurrent is present even when the phase difference is zero.

The physics of the 'short' NH-TIJJ described in this paper can be realized in practical devices, such as Nb-superconductors on the surface of a HgTe 3DTI [34], with dissipation introduced by attaching a 'lossy' metallic lead [14, 21] at the junction. For such a setup, relevant parameters include $\Delta \simeq 1$ meV, $\Gamma_0 \simeq 0.2$ meV, $\hbar v_F \simeq 250 - 350$ meV-nm and the junction width $< 1.25 - 1.75$
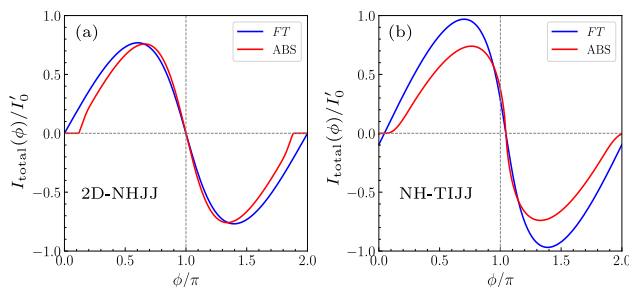

FIG. 5. **Comparison of the CPR obtained from the FT formula (Eq. (8)) and the ABS formula (Eq. (11)) for a complex barrier ($Z_1 = 0.4$ and $Z_2 = 0.2$):** (a) Planar ordinary NH-JJ, and (b) NH-TIJJ in the strong-proximity regime.

μm [34]. Another promising platform is Nb-Bi$_2$Te$_3$-Nb JJs [35, 36]. Since the length of the TIJJ qualitatively changes the CPR [37], a natural future direction is to investigate the effect of dissipation on quantum transport in a 'long' NH-TIJJ which will be explored in a separate study. Our findings thus highlight the effect of dissipation on the Josephson current in a topological Josephson junction, providing critical insights into the experimental realization of dissipation-engineered hybrid quantum devices and paving the way for leveraging non-Hermitian effects in TIJJs to advance quantum computing architectures.

Appendix A: Lindblad formalism to describe dissipation due to the normal lead

To investigate the impact of coupling a 'lossy' metallic lead at the junction to an electron reservoir on the transport properties of a TIJJ, we model the system as an open quantum system interacting with its environment, following Ref. [16]. The total Hamiltonian can be decomposed as $H = H_0 + H_E + H_c$, where H_0 is the system Hamiltonian, H_E describes the environment, and H_c represents the coupling between the system and environment. The dissipative dynamics induced by this coupling term can be described by the Lindblad master equation [23, 24, 38, 39]:

$$\frac{d\rho_0}{dt} = -i[H_0, \rho_0] + \sum_m \eta \left(\hat{\mathcal{L}}_m \rho_0 \hat{\mathcal{L}}_m^\dagger - \frac{1}{2}\{\hat{\mathcal{L}}_m \hat{\mathcal{L}}_m^\dagger, \rho_0\} \right). \tag{A1}$$

Here, ρ_0 is the reduced density matrix of the system, $\hat{\mathcal{L}}_m$ is the Lindblad (quantum jump) operator, and $\eta > 0$ is the dissipation rate. Rearranging this equation yields:

$$\frac{d\rho_0}{dt} = -i(H_{\text{eff}}\rho_0 - \rho_0 H_{\text{eff}}^\dagger) + \sum_m \eta \hat{\mathcal{L}}_m \rho_0 \hat{\mathcal{L}}_m^\dagger , \tag{A2}$$

where, the effective Hamiltonian is

$$H_{\text{eff}} = H_0 - \frac{i}{2} \sum_m \eta \hat{\mathcal{L}}_m \hat{\mathcal{L}}_m^\dagger . \tag{A3}$$

The non-Hermitian term $-\frac{i}{2}\sum_m \eta \hat{\mathcal{L}}_m \hat{\mathcal{L}}_m^\dagger$ accounts for the 'loss' due to coupling with the environment. By neglecting quantum jumps in the second term on the right-hand side of Eq. (A2), the system's dynamics can be effectively described by H_{eff} [16, 22]. This motivates modeling the non-Hermiticity introduced by the 'lossy' lead in the TIJJ by an imaginary potential term $-iV_2$ where $V_2 > 0$ is real.

Appendix B: Wavefunctions and bound states for NH-TIJJs

The wavefunctions for the two regions $x < 0$ (x_-) and $x > 0$ (x_+) of the NH-TIJJ, within the Andreev approximation and considering the limit of large Fermi energy ($\mu \gg \tilde{\Delta}(\epsilon)$), obtained by solving Eq. (2) have the forms [8],

$$\psi_{k_y}(x_+) = A \begin{bmatrix} 1 \\ e^{i\theta} \\ -e^{i\theta}a_R^+ \\ a_R^+ \end{bmatrix} e^{ik_F x \cos(\theta) - x/\xi}$$
$$+ B \begin{bmatrix} 1 \\ -e^{-i\theta} \\ e^{-i\theta}a_R^- \\ a_R^- \end{bmatrix} e^{-ik_F x \cos(\theta) - x/\xi} , \tag{B1}$$

$$\psi_{k_y}(x_-) = C \begin{bmatrix} 1 \\ e^{i\theta} \\ -e^{i\theta}a_L^- \\ a_L^- \end{bmatrix} e^{ik_F x \cos(\theta) + x/\xi}$$
$$+ D \begin{bmatrix} 1 \\ -e^{-i\theta} \\ e^{-i\theta}a_L^+ \\ a_L^+ \end{bmatrix} e^{-ik_F x \cos(\theta) + x/\xi}, \tag{B2}$$

where, A, B, C and D are constants, and k_F is the Fermi wavevector. The Andreev reflection amplitudes for the electron-like $(+)$ and hole-like $(-)$ quasiparticles are,

$$a_{L,R}^\pm(\epsilon) = \frac{\tilde{\Delta}(\epsilon)e^{-i\phi_{L,R}}}{\mathcal{E}(\epsilon) \pm i\sqrt{\tilde{\Delta}^2(\epsilon) - \mathcal{E}^2(\epsilon)}} , \tag{B3}$$

$$\cos(\theta) = \sqrt{1 - \left(\frac{k_y}{k_F}\right)^2}, \quad \mathcal{E}(\epsilon) = \epsilon + i\Gamma(\epsilon) . \tag{B4}$$

Inserting Eqs. (B1) and (B2) in Eq. (3), we get a set of four equations for A, B, C and D. For non-trivial solutions, the determinant of the coefficients of this system of equations must vanish, leading to following equation
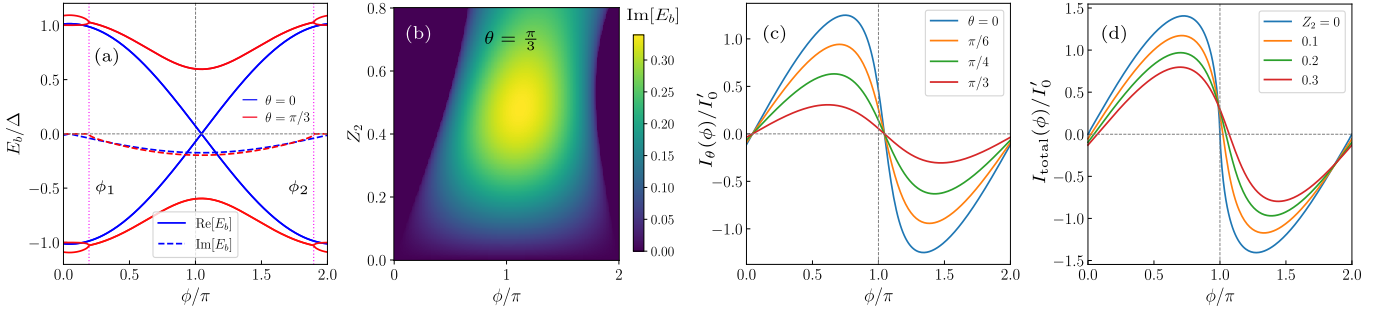
FIG. 6. **Characteristics of the NH-TIJJ in the strong-proximity limit ($\Gamma_0 = \Delta$):** (a) The real (solid lines) and imaginary (dashed lines) parts of the Andreev spectrum of the NH-TIJJ as a function of the phase difference ϕ plotted for different angles of incidence θ. (b) Variation of the imaginary part of the spectrum as a function of ϕ and Z_2 for the incident angle $\theta = \pi/3$, the boundary of the dark purple region demonstrates the asymmetric gap-exit points in the spectrum. (c) The angle-resolved current $I_\theta(\phi)$ plotted as a function of ϕ for different angles of incidence. (d) The total supercurrent $I_{\text{total}}(\phi)$ as a function of ϕ for different barrier parameters. The current is computed in units of $e\Delta/\hbar$ and we have chosen the real barrier parameter $Z_1 = 0.4$ and the imaginary barrier parameter $Z_2 = 0.2$

for the ABS energy:

$$T_1(a_L^+ a_L^- + a_R^+ a_R^-) - T_2(a_L^+ a_R^+ + a_L^- a_R^-) +$$
$$T_3(a_L^- a_R^+ + a_L^+ a_R^-) - 2iZ_1 Z_2 \cos^2(\theta)(a_L^+ a_L^- - a_R^+ a_R^-)$$
$$+ 2Z_2 \cos(\theta)(a_L^+ a_R^+ - a_L^- a_R^-) = 0 . \quad \text{(B5)}$$

where $T_1 = (1 + Z_1^2 - Z_2^2)\cos^2(\theta)$, $T_2 = Z_1^2 + Z_2^2 + \cos^2(\theta)$ and $T_3 = \sin^2(\theta)(Z_1^2 + Z_2^2)$. Substituting the coefficients from Eq. (B3) in Eq. (B5) we arrive at Eq. (4). Now from Eq. (5), denoting the R.H.S as $\mathcal{S}(\theta, \phi)$ and simplifying the L.H.S we obtain the following equation which can be rearranged to get Eq. (6),

$$\left(\frac{\epsilon}{\Delta} + \frac{\epsilon}{\Gamma_0} \sqrt{1 - \frac{\epsilon^2}{\Delta^2}} \right)^2 = \mathcal{S}(\theta, \phi) . \quad \text{(B6)}$$

Substituting the form: $|\epsilon/\Delta| = c_1 \gamma + c_2 \gamma^2 + c_3 \gamma^3$, in Eq. (6) and equating the coefficients of different powers in γ, we obtain

$$c_1 = -c_2 = \mathcal{S}^{\frac{1}{2}}(\theta, \phi),$$
$$c_3 = \mathcal{S}^{\frac{1}{2}}(\theta, \phi) + \frac{1}{2}\mathcal{S}^{\frac{3}{2}}(\theta, \phi). \quad \text{(B7)}$$

For the NH-TIJJ in the strong-proximity limit ($\Gamma_0 = \Delta$), the Andreev spectrum is shown in Fig. 6(a) and (b) and bears similarities in qualitative behaviors with that of the tunneling limit (see Fig. 2). This includes features like the spectrum bifurcation and asymmetry of the GEPs, note that for the strong-proximity limit the bifurcation happens around the parent superconducting gap Δ with one branch going above Δ and another below it, whereas in the tunneling limit the bifurcation occurs around the induced gap which is much smaller than Δ. Similarly, the angle-resolved current (Fig. 6(c)) and the total current CPR (Fig. 6(d)) exhibit the anomalous behavior stemming from the asymmetry of the spectrum.

Appendix C: Hamiltonian and bound states for an 'ordinary' NH-JJ

The BdG Hamiltonian for the 'ordinary' NH-JJ (3DTI in Fig. 1 is replaced by a 3D metal), in the same way as Eq. (2) in the main text, can be written as,

$$H_{\text{BdG}}^{(0)} = \begin{bmatrix} \hat{h}_0 - \mu + U(x) & \Delta' e^{i\phi_{L,R}} \\ \Delta' e^{-i\phi_{L,R}} & -(\hat{h}_0 - \mu + U^*(x)) \end{bmatrix} \quad \text{(C1)}$$

Here, $\hat{h}_0 = -\frac{\hbar^2}{2m}(\partial_x^2 + \partial_y^2)$ is the kinetic energy operator, m is the mass of electron, μ is the chemical potential of the superconductor and $U(x)$ is the complex potential barrier. The induced pair potential Δ' is assumed to be energy independent.

The wavefunctions for the bound states are obtained by solving for the eigenstates of $H_{\text{BdG}}^{(0)}$ in Eq. (C1). Within the Andreev approximation ($k_h = k_e^* \simeq k_F$) and taking p_y is a good quantum number, the general forms of the wavefunctions are given by: $\Psi(\mathbf{r}) = \sum_{k_y} \psi_{k_y}(x)e^{ik_y y}$, where,

$$\psi_{k_y}(x_-) = A_1 e^{ik_h x \cos(\theta)} \begin{pmatrix} v \\ u \end{pmatrix} + B_1 e^{-ik_e x \cos(\theta)} \begin{pmatrix} u \\ v \end{pmatrix} ,$$

$$\psi_{k_y}(x_+) = C_1 e^{ik_e x \cos(\theta)} \begin{pmatrix} u e^{\frac{i\phi}{2}} \\ v e^{-\frac{i\phi}{2}} \end{pmatrix}$$

$$+ D_1 e^{-ik_h x \cos(\theta)} \begin{pmatrix} v e^{\frac{i\phi}{2}} \\ u e^{-\frac{i\phi}{2}} \end{pmatrix} ,$$

$$u = \sqrt{\frac{1}{2}\left(1 + \frac{i\sqrt{\Delta'^2 - \epsilon^2}}{\epsilon}\right)} ,$$

$$v = \sqrt{\frac{1}{2}\left(1 - \frac{i\sqrt{\Delta'^2 - \epsilon^2}}{\epsilon}\right)} ,$$

where, $\cos(\theta) = \sqrt{1 - (k_y/k_F)^2}$. The boundary conditions for the wavefunctions on either side of the junctions are,

$$\Psi_-(0) = \Psi_+(0) \,,$$
$$\Psi'_+(0) - \Psi'_-(0) = -\frac{2m}{\hbar^2}(iV_1\tau_0 + V_2\tau_z)\Psi(0) \,. \quad \text{(C2)}$$

The boundary conditions in Eq. (C2) lead to four sets of equations for the amplitudes A_1, B_1, C_1 and D_1. For a non-trivial solution the determinant of the characteristic equation must be zero from which we obtain the secular equation to determine the ABS energy to be,

$$\frac{\Delta'^2}{\epsilon^2}(Z^2 + \cos^2(\theta)\cos^2(\phi/2))$$
$$- 2iZ_2\cos(\theta)\sqrt{\frac{\Delta'^2}{\epsilon^2} - 1} - (Z^2 + \cos^2(\theta)) = 0 \,. \quad \text{(C3)}$$

Solving the above Eq. (C3) for $y = \epsilon^2/\Delta'^2$, we obtain the expression of ABS energy in Eq. (10).

[1] E. L. Wolf, G. B. Arnold, M. A. Gurvitch, and J. F. Zasadzinski, *Josephson junctions: history, devices, and applications* (CRC Press, 2017).

[2] B. D. Josephson, The discovery of tunnelling supercurrents, Rev. Mod. Phys. **46**, 251 (1974).

[3] E. D. Walsh, W. Jung, G.-H. Lee, D. K. Efetov, B.-I. Wu, K.-F. Huang, T. A. Ohki, T. Taniguchi, K. Watanabe, P. Kim, D. Englund, and K. C. Fong, Josephson junction infrared single-photon detector, Science **372**, 409 (2021).

[4] L. Fu and C. L. Kane, Superconducting proximity effect and majorana fermions at the surface of a topological insulator, Phys. Rev. Lett. **100**, 096407 (2008).

[5] J. Cayao, P. Dutta, P. Burset, and A. M. Black-Schaffer, Phase-tunable electron transport assisted by odd-frequency cooper pairs in topological josephson junctions, Phys. Rev. B **106**, L100502 (2022).

[6] P. Dutta, Phase-dependent charge and heat current in thermally biased short josephson junctions formed at helical edge states, New Journal of Physics **25**, 083024 (2023).

[7] P. Dutta, J. Cayao, A. M. Black-Schaffer, and P. Burset, Nonlocality of majorana bound states revealed by electron waiting times in a topological andreev interferometer, Phys. Rev. Res. **6**, L012062 (2024).

[8] G. Tkachov and E. M. Hankiewicz, Helical andreev bound states and superconducting klein tunneling in topological insulator josephson junctions, Phys. Rev. B **88**, 075401 (2013).

[9] C. T. Olund and E. Zhao, Current-phase relation for josephson effect through helical metal, Phys. Rev. B **86**, 214515 (2012).

[10] M. Z. Hasan and C. L. Kane, Colloquium: Topological insulators, Rev. Mod. Phys. **82**, 3045 (2010).

[11] X.-L. Qi and S.-C. Zhang, Topological insulators and superconductors, Rev. Mod. Phys. **83**, 1057 (2011).

[12] L. Fu and C. L. Kane, Josephson current and noise at a superconductor/quantum-spin-hall-insulator/superconductor junction, Phys. Rev. B **79**, 161408 (2009).

[13] J. Wiedenmann, E. Bocquillon, R. S. Deacon, S. Hartinger, O. Herrmann, T. M. Klapwijk, L. Maier, C. Ames, C. Brüne, C. Gould, *et al.*, 4 π-periodic josephson supercurrent in hgte-based topological josephson junctions, Nature communications **7**, 10303 (2016).

[14] J. Cayao and M. Sato, Non-hermitian phase-biased josephson junctions, Phys. Rev. B **110**, L201403 (2024).

[15] V. Kornich, Current-voltage characteristics of the normal metal-insulator-pt-symmetric non-hermitian superconductor junction as a probe of non-hermitian formalisms, Phys. Rev. Lett. **131**, 116001 (2023).

[16] C.-A. Li, H.-P. Sun, and B. Trauzettel, Anomalous andreev spectrum and transport in non-hermitian josephson junctions, Phys. Rev. B **109**, 214514 (2024).

[17] P.-X. Shen, Z. Lu, J. L. Lado, and M. Trif, Non-hermitian fermi-dirac distribution in persistent current transport, Phys. Rev. Lett. **133**, 086301 (2024).

[18] J. Cayao and M. Sato, Non-hermitian multiterminal phase-biased josephson junctions, Phys. Rev. B **110**, 235426 (2024).

[19] C. W. J. Beenakker, Josephson effect in a junction coupled to an electron reservoir, Applied Physics Letters **125**, 122601 (2024).

[20] D. M. Pino, Y. Meir, and R. Aguado, Thermodynamics of non-hermitian josephson junctions with exceptional points, Phys. Rev. B **111**, L140503 (2025).

[21] D. C. Ohnmacht, V. Wilhelm, H. Weisbrich, and W. Belzig, Non-hermitian topology in multiterminal superconducting junctions, arXiv preprint arXiv:2408.01289 (2024).

[22] P. M. Harrington, E. J. Mueller, and K. W. Murch, Engineered dissipation for quantum information science, Nature Reviews Physics **4**, 660 (2022).

[23] H.-P. Breuer and F. Petruccione, *The theory of open quantum systems* (Oxford University Press, USA, 2002).

[24] A. J. Daley, Quantum trajectories and open many-body quantum systems, Advances in Physics **63**, 77 (2014).

[25] A. C. Potter and P. A. Lee, Engineering a $p+ip$ superconductor: Comparison of topological insulator and rashba spin-orbit-coupled materials, Phys. Rev. B **83**, 184520 (2011).

[26] M. Lababidi and E. Zhao, Microscopic simulation of superconductor/topological insulator proximity structures, Phys. Rev. B **83**, 184511 (2011).

[27] G. Tkachov and E. M. Hankiewicz, Spin-helical transport in normal and superconducting topological insulators, physica status solidi (b) **250**, 215 (2013).

[28] R. Capecelatro, M. Marciani, G. Campagnano, and P. Lucignano, Andreev non-hermitian hamiltonian for open josephson junctions from green's functions, Phys. Rev. B **111**, 064517 (2025).

[29] V. Kornich and B. Trauzettel, Andreev bound states in junctions formed by conventional and $\mathcal{PT}$-symmetric non-hermitian superconductors, Phys. Rev. Res. **4**, 033201 (2022).

[30] T.-S. Deng, L. Pan, Y. Chen, and H. Zhai, Stability of time-reversal symmetry protected topological phases, Phys. Rev. Lett. **127**, 086801 (2021).

[31] S. Datta, *Electronic transport in mesoscopic systems* (Cambridge university press, 1997).

[32] A. Furusaki and M. Tsukada, Dc josephson effect and andreev reflection, Solid State Communications **78**, 299 (1991).

[33] B. Lu and Y. Tanaka, Study on green's function on topo-

logical insulator surface, Philosophical Transactions of the Royal Society A: Mathematical, Physical and Engineering Sciences **376**, 20150246 (2018).

[34] L. Maier, J. B. Oostinga, D. Knott, C. Brüne, P. Virtanen, G. Tkachov, E. M. Hankiewicz, C. Gould, H. Buhmann, and L. W. Molenkamp, Induced superconductivity in the three-dimensional topological insulator hgte, Phys. Rev. Lett. **109**, 186806 (2012).

[35] V. S. Stolyarov, D. Roditchev, V. L. Gurtovoi, S. N. Kozlov, D. S. Yakovlev, O. V. Skryabina, V. M. Vinokur, and A. A. Golubov, Resonant oscillations of josephson current in Nb-$Bi_2Te_{2.3}Se_{0.7}$-Nb junctions, Advanced Quantum Technologies **5** (2022).

[36] S. Charpentier, L. Galletti, G. Kunakova, R. Arpaia, Y. Song, R. Baghdadi, S. M. Wang, A. Kalaboukhov, E. Olsson, F. Tafuri, *et al.*, Induced unconventional superconductivity on the surface states of bi2te3 topological insulator, Nature Communications **8**, 2019 (2017).

[37] B. Lu, S. Ikegaya, P. Burset, Y. Tanaka, and N. Nagaosa, Tunable josephson diode effect on the surface of topological insulators, Phys. Rev. Lett. **131**, 096001 (2023).

[38] F. Roccati, G. M. Palma, F. Ciccarello, and F. Bagarello, Non-hermitian physics and master equations, Open Systems & Information Dynamics **29**, 2250004 (2022).

[39] D. Manzano, A short introduction to the Lindblad master equation, AIP Advances **10**, 025106 (2020).